Radiation heat transfer model for complex superalloy turbine blade in directional solidification process based on finite element method

Dun-ming Liao, Liu Cao, Tao Chen, Fei Sun, Yong-zhen Jia, Zi-hao Teng and Yu-long Tang

State Key Laboratory of Materials Processing and Die & Mould Technology, Huazhong University of Science and Technology, Wuhan 430074, China

Abstract: For the sake of a more accurate shell boundary and calculation of radiation heat transfer in the Directional Solidification (DS) process, a radiation heat transfer model based on the Finite Element Method (FEM) is developed in this study. Key technologies, such as distinguishing boundaries automatically, local matrix and lumped heat capacity matrix, are also stated. In order to analyze the effect of withdrawing rate on DS process, the solidification processes of a complex superalloy turbine blade in the High Rate Solidification (HRS) process with different withdrawing rates are simulated; and by comparing the simulation results, it is found that the most suitable withdrawing rate is determined to be 5.0 mm•min^{-1}. Finally, the accuracy and reliability of the radiation heat transfer model are verified, because of the accordance of simulation results with practical process.

Key words: Directional solidification; radiation heat transfer; finite element method; numerical simulation; local matrix; superalloy turbine blade

CLC numbers: TG249   **Document code:** A   **Article ID:** 1672-6421(2016)02-123-10

With the development of the aviation industry, the turbine blade, as the most critical component of the aero-engine, has received more and more attention. At present, most turbine blades are made of superalloy material and produced by the Directional Solidification (DS) technology [1-4]. In recent years, computer simulation technology has played a more and more important role in the DS process, including the simulation of macroscopic physical fields[5-10] and microstructure[11-14]. In the field of numerical simulation in the DS process, the Finite Difference Method (FDM)[15] and Finite Element Method (FEM)[16] are two of the most common numerical methods. FEM is suitable for unstructured mesh. Hong et al.[17,18] simulated the temperature field in the DS process by ProCAST software (ESI Group, Paris, France), which is based on tetrahedral mesh, but the computation efficiency was low. In order to improve the calculation efficiency, Cui et al.[19,20] developed an improved Monte Carlo ray tracing approach to calculate radiation heat transfer, but the mesh solution couldn't accurately match with the irregular shuttering by FDM.

Considering that the irregular shell boundary and radiation heat transfer need to be handled in numerical simulation of the DS process, an improved Monte Carlo ray tracing approach is used to calculate radiation heat transfer, and a radiation heat transfer model based on FEM is explained. The key technologies, such as distinguishing boundaries automatically, local matrix and lumped heat capacity matrix, are also expounded. Through the work above, a temperature-field numerical simulative program of DS based on the FEM is developed. By calculating the temperature fields of a superalloy turbine blade in HRS process with different withdrawing rates [21, 22], the effects of different withdrawing rates on the DS process, such as temperature gradient, cooling rate and solidification rate, are analyzed, and the HRS technology is also optimized.

*Dun-ming Liao

Male, born in 1973, Professor, Doctor of engineering, Doctoral supervisor. His research focuses on the digital studies of casting process. His academic research has led to the publication of more than 45 papers.

Corresponding author: Tao Chen, e-mail: cht1399@foxmail.com

1 Mathematical modeling

1.1 Governing equations

Heat conduction equation, which is deduced from Fourier heat equation and the law of conservation of energy, is the basic equation describing heat transfer

process. The differential equation that the field variable $\phi(x,y,z,t)$ of transient temperature field in three dimensions under Cartesian coordinate system should satisfy [23]:

$$\rho c \frac{\partial \phi}{\partial t} - \nabla \cdot (k\nabla\phi) - \rho Q = 0 \qquad (1)$$

where ρ is the density, c is the specific heat, t is the time, k is the thermal conductivity, and Q is the inner heat source density.

It is necessary to note that a radiation heat transfer model is paid the most attention in this study, so some assumptions are made in the simulation, including the overlook of flow of liquid and transport of solute. On account of the release of latent heat, the heat transfer process inside the casting can actually be treated as a temperature field with inner heat source. The latent heat is handled by equivalent specific heat method, in which the latent heat is supposed to be released uniformly between liquidus temperature and solidus temperature, and temperature correction is needed afterwards. Therefore, the specific heat c, in Eq. 1, can be replaced by the equivalent specific heat c_p [24], which is determined by:

$$c_p = \begin{cases} c + \dfrac{L}{\phi_L - \phi_S} & \phi_S \leq \phi \leq \phi_L \\ c & \phi > \phi_L \quad or \quad \phi < \phi_S \end{cases} \qquad (2)$$

where L is the latent heat, ϕ_L is the liquidus temperature, and ϕ_S is the solidus temperature.

1.2 Boundary of radiation heat transfer

As radiation heat distributes in three-dimensional space, it needs to be discretized on the physical level, and ray tracing is needful before dealing with the boundary of radiation heat transfer. Because of the complexity of DS process, including the radiation baffle, the water cooling crystallizer, and the drawing motion of casting and shell, more attention must be paid to the boundary of radiation heat transfer.

The physical discretization method for the boundary of radiation heat transfer is an improved Monte Carlo ray tracing approach [19]. Figure 1 shows the thinking of physical discretization that the upper hemisphere space is divided into multi subspaces, each of which is replaced by several corresponding rays, and the final location of each ray should be recorded in order to gain the element j shot by the ray and its temperature ϕ_j. It should be made clear that the radiation energy represented by each ray is supposed to be absorbed totally by the element j, so the radiation angle factor φ_j is equal to the constant one.

The subspace represented by a ray can be determined by the angle α with the X axis, the horizontal included angle $\Delta\alpha$, the angle β with the Z axis and the vertical included angle $\Delta\beta$. By summing the radiation energy of each subspace, the total radiation energy Q_{rad} between the surface element and the outside can be determined as:
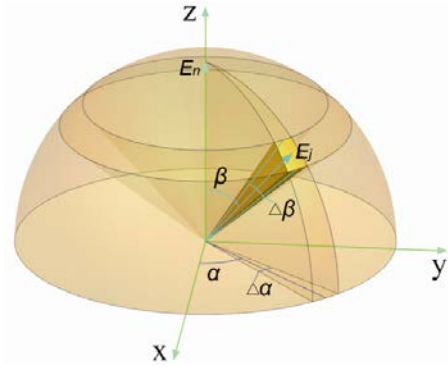

Fig. 1: Schematic diagram of physical discretization for the boundary of radiation heat transfer

$$Q_{rad} = \sum_{j=1}^{n} Q_j \qquad (3)$$

$$Q_j = \eta_j \sigma (\phi^4 - \phi_j^4) / (\frac{1-\varepsilon}{\varepsilon} \cdot \frac{1}{S} + \frac{1-\varepsilon_j}{\varepsilon_j} \cdot \frac{1}{S_j} + \frac{1}{S}) \qquad (4)$$

where n is the number of the subspaces, ε and ε_j are the blackness of materials on the ray's origin and endpoint respectively, S and S_j are the area of elements on the ray's origin and endpoint respectively, σ is the Stefan-Boltzman constant and η_j is the radiant weight factor which is applied to express the ratio between the radiation force represented by the ray j and the total radiation force of the surface element.

According to the Lambert law, the directional radiation force in three-dimensional space can be expressed as:

$$E_\beta = E_n \cdot \cos\beta \qquad (5)$$

where E_n is the radiation force of the normal ray and E_β is the radiation force of the ray with the included angle β relative to the normal direction.

The total radiation force of the surface element can be determined as:

$$E = \int_0^{\frac{\pi}{2}} \int_0^{2\pi} E_\beta dS = \int_0^{\frac{\pi}{2}} \int_0^{2\pi} E_n \cdot \cos\beta \cdot r \sin\beta \cdot d\beta \cdot r d\alpha = \pi r^2 E_n \qquad (6)$$

where r is the distance between the surface element and the subspace's infinitesimal element.

The radiation force of the subspace can be gotten by the integral operation, as follows:

$$E_j = \int_{\beta-\frac{\Delta\beta}{2}}^{\beta+\frac{\Delta\beta}{2}} \int_{\alpha-\frac{\Delta\alpha}{2}}^{\alpha+\frac{\Delta\alpha}{2}} E_\beta dS = \frac{r^2 E_n \Delta\alpha}{4}[\cos(2\beta-\Delta\beta) - \cos(2\beta+\Delta\beta)] \qquad (7)$$

So the radiant weight factor can be determined by:

$$\eta_j = \frac{E_j}{E} = \frac{\Delta\alpha}{4\pi} \cdot [\cos(2\beta-\Delta\beta) - \cos(2\beta+\Delta\beta)] \qquad (8)$$

The radiation heat transfer is applied to the surface element, so the boundary condition of radiation heat transfer can be

formulated as:

$$k \frac{\partial \phi}{\partial x} n_x + k \frac{\partial \phi}{\partial y} n_y + k \frac{\partial \phi}{\partial z} n_z = -\frac{Q_{rad}}{S} \quad (9)$$

where n_x, n_y and n_z are the direction cosines of the surface element's exterior normal.

By substitution of Eq. 3, Eq. 4 and Eq. 8 into Eq. 9, the following equation results:

$$k \frac{\partial \phi}{\partial x} n_x + k \frac{\partial \phi}{\partial y} n_y + k \frac{\partial \phi}{\partial z} n_z$$
$$= \sum_{j=1}^{n} [\eta_j \cdot \sigma \cdot \phi_j^4 / (\frac{1}{\varepsilon} + \frac{1-\varepsilon_j}{\varepsilon_j} \cdot \frac{S}{S_j})] - \phi^4 \sum_{j=1}^{n} [\eta_j \cdot \sigma / (\frac{1}{\varepsilon} + \frac{1-\varepsilon_j}{\varepsilon_j} \cdot \frac{S}{S_j})] \quad (10)$$

Hypothesizing that:

$$M_0 = \sum_{j=1}^{n} [\eta_j \cdot \sigma \cdot \phi_j^4 / (\frac{1}{\varepsilon} + \frac{1-\varepsilon_j}{\varepsilon_j} \cdot \frac{S}{S_j})] \quad (11)$$

$$M_1 = \sum_{j=1}^{n} [\eta_j \cdot \sigma / (\frac{1}{\varepsilon} + \frac{1-\varepsilon_j}{\varepsilon_j} \cdot \frac{S}{S_j})] \quad (12)$$

Thereupon, Eq. 10 can be rewritten as:

$$k \frac{\partial \phi}{\partial x} n_x + k \frac{\partial \phi}{\partial y} n_y + k \frac{\partial \phi}{\partial z} n_z = M_0 - M_1 \cdot \phi^4 \quad (13)$$

After the linearization process to right-hand member of Eq. 13 with the formula of expanded Taloy series, it can be restated as follows:

$$k \frac{\partial \phi}{\partial x} n_x + k \frac{\partial \phi}{\partial y} n_y + k \frac{\partial \phi}{\partial z} n_z = M_0 + 3M_1 \phi_e^4 - 4M_1 \phi_e^3 \phi \quad (14)$$

where ϕ_e is the average temperature of surface element.

Hypothesizing that:

$$D_0 = M_0 + 3M_1 \phi_e^4$$
$$= \sum_{j=1}^{n} [\eta_j \cdot \sigma \cdot \phi_j^4 / (\frac{1}{\varepsilon} + \frac{1-\varepsilon_j}{\varepsilon_j} \cdot \frac{S}{S_j})] + 3\phi_e^4 \cdot \sum_{j=1}^{n} [\eta_j \cdot \sigma / (\frac{1}{\varepsilon} + \frac{1-\varepsilon_j}{\varepsilon_j} \cdot \frac{S}{S_j})] \quad (15)$$

$$D_1 = 4M_1 \phi_e^3 = 4\phi_e^3 \cdot \sum_{j=1}^{n} [\eta_j \cdot \sigma / (\frac{1}{\varepsilon} + \frac{1-\varepsilon_j}{\varepsilon_j} \cdot \frac{S}{S_j})] \quad (16)$$

Hence, Eq. 14 can be replaced by:

$$k \frac{\partial \phi}{\partial x} n_x + k \frac{\partial \phi}{\partial y} n_y + k \frac{\partial \phi}{\partial z} n_z = D_0 - D_1 \phi \quad (17)$$

It should be stated that the above equations use the representation of absolute temperature, so Eq. 17 can be altered as:

$$k \frac{\partial \phi}{\partial x} n_x + k \frac{\partial \phi}{\partial y} n_y + k \frac{\partial \phi}{\partial z} n_z = D_0 - D_1 (\phi + 273.15) \quad (18)$$

By analyzing Eq. 18, it is easy to discover that the boundary condition of radiation heat transfer has the same form of the boundary condition of heat convection, so the boundary condition of radiation heat transfer is regarded as a special boundary condition of heat convection in the program.

1.3 Boundary of heat convection

The boundary condition of heat convection[25] is formulated as:

$$k \frac{\partial \phi}{\partial x} n_x + k \frac{\partial \phi}{\partial y} n_y + k \frac{\partial \phi}{\partial z} n_z = h (\phi_a - \phi) \quad (19)$$

where h is the interface heat-transfer coefficient and ϕ_a is the external temperature.

By Eq. 19, contact relations among the boundaries should be confirmed before handling the boundary of heat convection. In order to preven tedious operations by selecting boundary elements manually, the diffusion element method is used to distinguish inner boundaries from outer boundaries. Figure 2 is the boundary schematic diagram of the casting and shell. Firstly, the top boundaries A1 and B1 can be obtained easily, so the remaining boundary of casting is the inner boundary A2. Then the nearest boundary element of shell from A2 needs to be determined among the remaining boundary elements of shell, and the connected elements can be found by the diffusion operation based on the nearest boundary element, so the inner boundary B2 and the outer boundary B3 of shell can be distinguished.
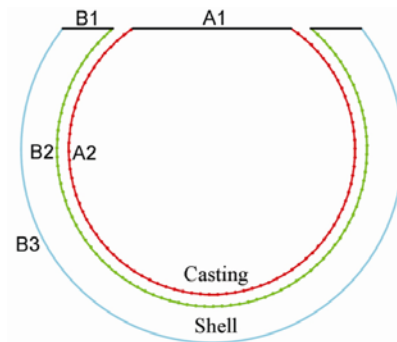

Fig. 2: Boundary schematic diagram of cast and shell

After confirming the inner and outer boundaries, the contact element for each inner boundary node can be sought by the box-tree method[23]. In allusion to the inner boundary node P, its subpoint P' can be gained on its contact triangle element ABC, then the local coordinate (t_1, t_2) of P' can be ascertained by establishing the local coordinate system on the element ABC, so the external temperature ϕ_a of node P can be determined by linear interpolation operation. Figure 3 is the interpolation schematic diagram of the external temperature.

$$\phi_a = (1 - t_1 - t_2) \phi_A + t_1 \phi_B + t_2 \phi_C \quad (20)$$

where ϕ_A, ϕ_B and ϕ_C are the temperatures of the contact element's three vertices.
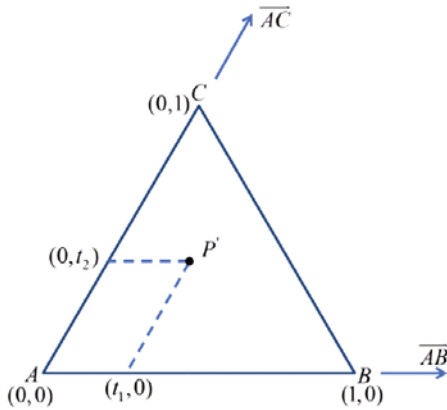
Fig. 3: Interpolation schematic diagram of external temperature

1.4 Calculation methodology

In light of the mathematical model and boundary treatment, the solving equation of unsteady temperature field in DS process can be described by FEM solving theory [26], as follows:

$$C\dot{\phi} + K\phi = N \tag{21}$$

where C is the specific heat matrix, K is the thermal conductivity matrix, N is the load vector, ϕ is the vector of nodal temperature and $\dot{\phi}$ is the vector of the derivative of nodal temperature with respect to time.

Solving matrix operation is required for Eq. 21, and the matrixes in Eq. 21 are supported to contain every material according to the common idea in FEM, resulting in low computational efficiency with large matrixes. Therefore, the concept of local matrix, which means to assemble the matrixes for each material independently, is proposed to raise the computational efficiency. Figure 4 is the schematic diagram showing global matrix and local matrix solutions. Moreover, the use of local matrix makes it possible to adopt different time steps for different materials. The resulting symmetric positive definite systems are solved by using preconditioned conjugate gradients [23].
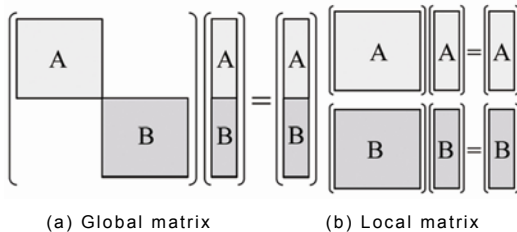

(a) Global matrix   (b) Local matrix

Fig. 4: Schematic diagram of local matrix

During the calculation process of an unsteady temperature field, the oscillation in time and space may appear, resulting from the discretization for governing equations that translates the problem with infinite degrees of freedom to the one with finite degrees of freedom. The discrete equation is rigid to some extent, causing the limited response speed. When the thermal load changes rapidly, the result may bring heat accumulating or reducing on some nodes [27].

A reasonable solution for the above issue is to concentrate the heat capacity of elements on nodes, considering that heat capacity only belongs to nodes[25]. A feasible approach is to add the elements of the same row or column of the heat capacity matrix together, instead of original diagonal elements, as Eq. 22 shows:

$$\begin{bmatrix} c_{11} & c_{12} & \cdots & c_{1n} \\ c_{21} & c_{22} & \cdots & c_{2n} \\ & \cdots & & \\ c_{n1} & c_{n2} & \cdots & c_{nn} \end{bmatrix} = \begin{bmatrix} c_{11}+c_{12}+\cdots+c_{1n} & 0 & \cdots & 0 \\ 0 & c_{21}+c_{22}+\cdots+c_{2n} & \cdots & 0 \\ & & \cdots & \\ 0 & 0 & \cdots & c_{n1}+c_{n2}+\cdots+c_{nn} \end{bmatrix} \tag{22}$$

The operation of lumped heat capacity matrix could be accomplished while assembling the heat capacity matrix. With regard to the linear tetrahedral element, the concentrated coefficient $\sum_{j=1}^{4}\int_{\Omega^e} N_iN_jd\Omega$ of each vertex i is 1/24 by gauss integration method [23]. Here, N_i is the shape function and Ω^e is the reference cell. For the quadratic tetrahedral element, the concentrated coefficient $\sum_{j=1}^{10}\int_{\Omega^e} N_iN_jd\Omega$ is -1/120 for four vertexes and 1/30 for six midpoints.

On the basis of the above FEM theory of unsteady temperature field and boundary treatment, a temperature-field numerical simulative program of DS based on FEM is developed by C++ computer language. Its solution flow chart is shown in Fig. 5.
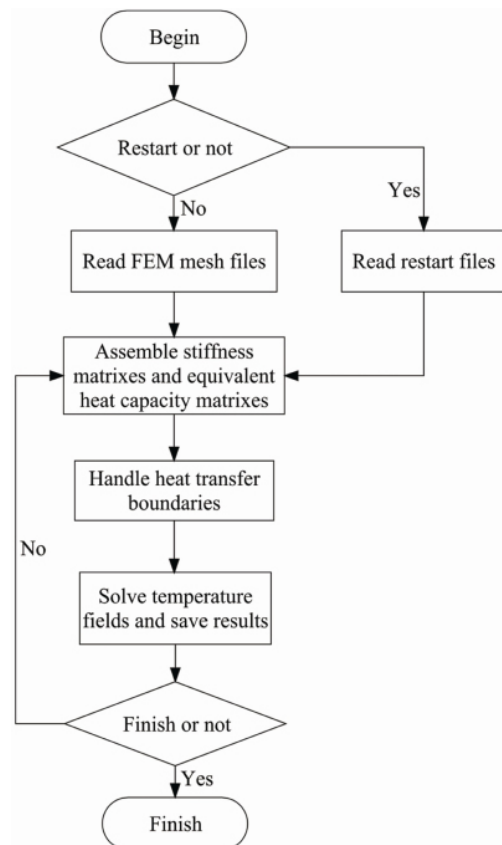

Fig. 5: Solving flow chart of temperature field program in DS process

2 Results and discussion

2.1 Feasibility analysis of mixed time step

The concept of local matrix which is proposed to raise the computational efficiency makes it possible to adopt different time steps for different materials. In order to verify the feasibility of mixed time step, three casting crafts with different mold complexities are chosen, as shown in Fig. 6.
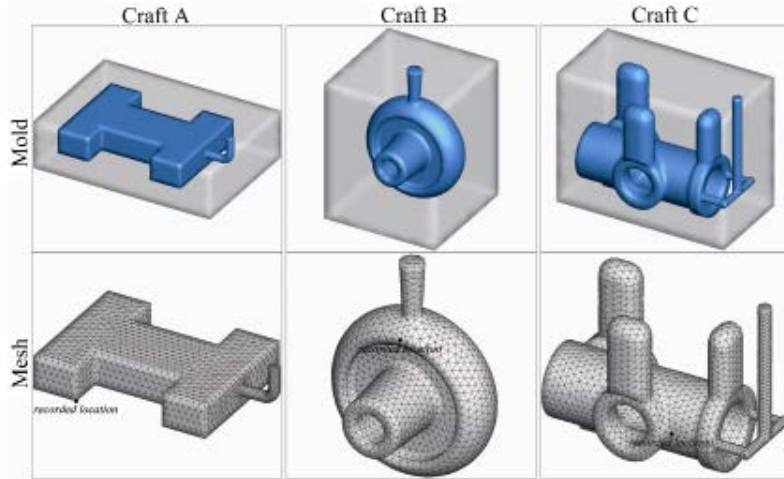

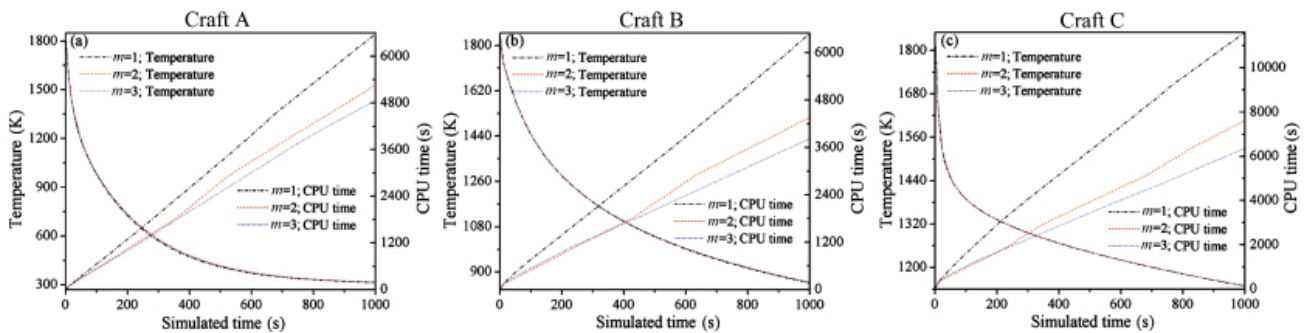**Fig. 6: Three casting crafts with different mold complexities**

The parameter m is the multiple between the time step of mould and casting, each craft was computed under the conditions of $m=1$, $m=2$ and $m=3$, and the other simulation parameters of the crafts are the same. The temperature changes of the recorded locations signed in Fig. 6 and CPU time of three crafts are recorded, as shown in Fig. 7. By the comparison of results, the CPU time reduces with m increasing, and the values of computed temperature have no performance difference. Comparing with the condition of $m=1$, the maximum percent of reduced CPU time for the three crafts are 26.05%, 41.03% and 45.15%. Therefore, mixed time step has a more effective effect on the computational efficiency, when the complexity of mold increases.

2.2 Model of superalloy turbine blade and simulation parameters

The shrouded turbine blade consists of four parts, including blade tips shroud, top platform, blade, and bottom platform, as shown in Fig. 8. After the addition of the gating system and the spiral grain selector based on the geometric

Fig. 7: Effect of mixed time step on computational efficiency
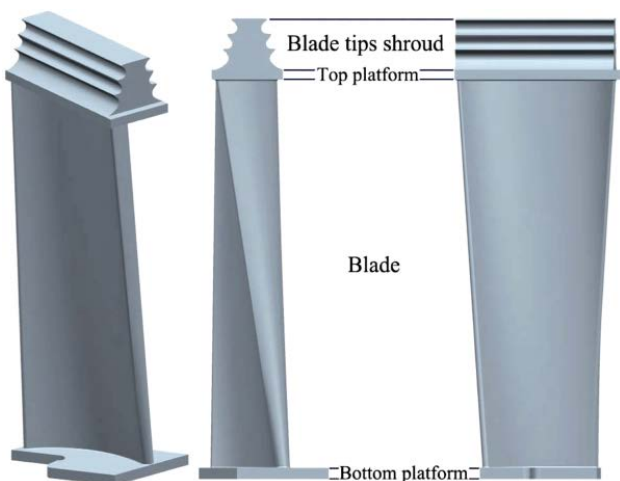
Fig. 8: Geometric model of shrouded turbine blade

model of shrouded turbine blade, the geometric model of the blade casting is shown in Fig. 9.

The blade casting was produced through the HRS technology, and Figure 10 shows the whole geometric and mesh model, including casting, shell, water cooled crystallizer, radiation baffle and furnace (consisting of heating zone and cooling zone). The mesh model was generated by the tetrahedral grid software of the author's laboratory. The mesh of shell, whose thickness is 3 mm, was obtained on the base of the casting and water cooled crystallizer mesh. Besides, the furnace only requires surface mesh. The element and node numbers of the whole mesh model are 92,080 and 26,320 respectively, which are 37,791 and 9,914 for the casting mesh.

The casting material is DD4 superalloy, the chemical compositions of which are 68.1% Ni, 9.0% Cr, 7.5%
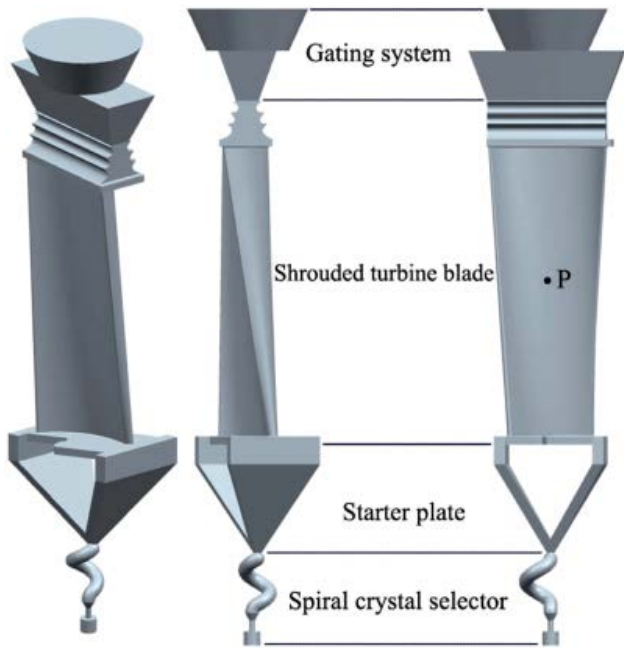
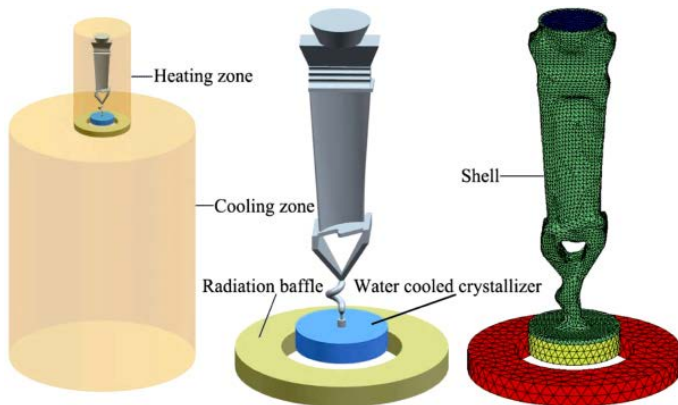**Fig. 9: Geometric model of blade casting**

Fig. 10: Whole geometric and mesh model of HRS technology

Co, 6.0% W, 1.5% Mo, 3.7% Al and 4.2% Ti in weight. The thermophysical parameters of DD4 superalloy computed by JMatPro software (Sente Software Ltd., Boston, UK) are shown in Table 1. The liquidus and solidus temperatures are 1,653 K (1,380 °C) and 1,553 K (1280 °C) respectively, and the latent heat is integrated in the specific heat term. The shell, radiation baffle and water cooled crystallizer adopt constant thermophysical parameters, as shown in Table 2. The convective heat transfer coefficients are 1,000 W•m^{-2}•K^{-1} between casting and shell, 1,000 W•m^{-2}•K^{-1} between casting and water cooled crystallizer and 500 W•m^{-2}•K^{-1} between shell and water cooled crystallizer. The wall temperatures of the heating zone and cooling zone are 1,833 K (1,560 °C) and 303 K (30 °C) respectively. The emissivity of furnace is 0.7, while the other components are uniformly 0.8. The temperature of the cooling

Table 1: Thermophysical parameters of DD4 superalloy computed by JMatPro

Temperature K (°C)	Density (kg•m^{-3})	Heat conductivity (W•m^{-1}•K^{-1})	Specific heat (J•kg^{-1}•K^{-1})
1,668 (1,395)	7,373	31.308	705
1,658 (1,385)	7,381	31.137	702
1,653 (1,380)	7,385	31.053	700
1,633 (1,360)	7,598	32.797	5,541
1,583 (1,310)	7,736	33.374	1,053
1,558 (1,285)	7,759	33.113	790
1,458 (1,185)	7,809	31.403	625
1,273 (1,000)	7,953	25.078	767
973 (700)	8,105	20.181	547
373 (100)	8,325	11.838	445

Table 2: Constant thermophysical parameters of shell, radiation baffle and water cooled crystallizer

| Material	Density (kg•m^{-3})	Heat conductivity (W•m^{-1}•K^{-1})	Specific heat (J•kg^{-1}•K^{-1})
Shell	2,500	2.1	1,180
Radiation baffle	1,600	16.2	1,540
Water cooled crystallizer	8,000	25.0	450

water under the bottom of water cooled crystallizer is always 303 K (30 °C), and the convective heat transfer coefficient is 4,000 W•m^{-2}•K^{-1} between them.

Considering that the withdrawing rate has the greatest influence on the DS process, two simulation schemes with different withdrawing rates are computed first. The withdrawing rate of two schemes are 4 and 8 mm•min^{-1} respectively. The pouring temperatures of both schemes isare 1,833 K (1,560 °C).

2.3 Simulation results and analyses

Before pouring molten metal, the other components should be preheated in actual HRS production. Figure 11 shows the final preheat temperature field computed by the program. From the simulation results, the final preheat temperature field presented gradient distribution from the bottom up for the influence of cooling water and cooling zone, benefiting the formation and directional growth of grain.

The solidification processes of HRS were computed on the basis of the final preheat temperature field, and the casting temperature and mushy zone fields of scheme 1 and scheme 2 are shown in Fig. 12 and Fig. 13, respectively. From the result of temperature fields, the radiation heat transfer between the shell and cooling zone intensified with the shell withdrawn from the heating zone gradually, forming the gradient distribution of casting temperature field. Comparing the mushy zone fields of scheme 1 and 2, the solidifying front of scheme 1 maintained horizontal distribution which contributed to the directional
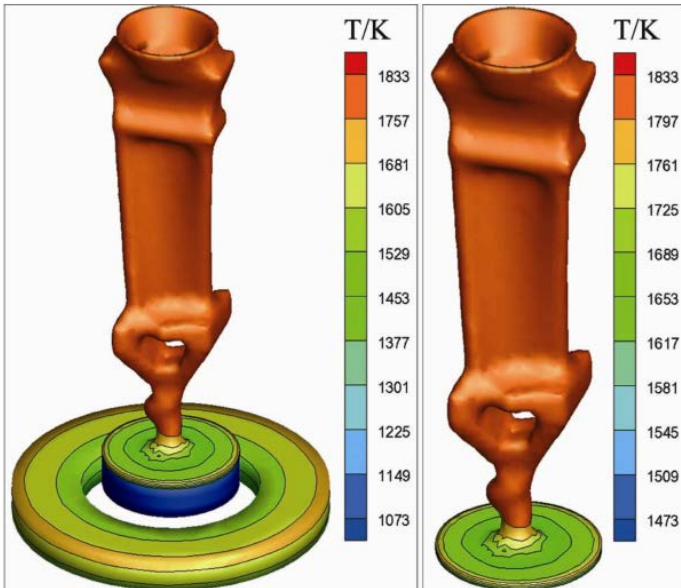
(a) The whole   (b) The shell

Fig. 11: Final preheat temperature field

growth of grain, however, the solidifying front of scheme 2 presented concave distribution which easily causes deflected grain, for the reason that , with the faster withdrawing rate, both sides of the blade cooled significantly faster than the

middle.Hence, the withdrawing rate should be reasonably controlled in order to achieve the directional growth of grain.

For the sake of the optimal withdrawing rate, seven simulation schemes with withdrawing rates between scheme 1 and scheme 2 were set and the withdrawing rates of scheme 3 to scheme 9 are 4.5, 5.0, 5.5, 6.0, 6.5, 7.0, 7.5 mm•min^{-1}, respectively.

The time t_c when each part of the casting cooled to the critical temperature ϕ_c were recorded to compare the solidification speeds under different withdrawing rates, in addition, ϕ_c is a particular value between the liquidus and solidus temperatures, which is set as below in this study:

$$\phi_c = \phi_S + (\phi_L - \phi_S) \times 0.1 \tag{23}$$

From the distribution of t_c under different withdrawing rates as shown in Fig. 14, the solidification sequence of casting in a certain scheme revealed an obvious longitudinal gradient distribution. Furthermore, the casting solidification time gradually shortened when the withdrawing rate increased.

A certain location P on the middle of the casting was chosen, as shown in Fig. 9, and the temperature gradient G, cooling rate R and solidification rate L of this location were computed, as shown in Fig. 15. The values of G, R and L all increased at first and then decreased with the increase in withdrawing rate. What is more, the maximum
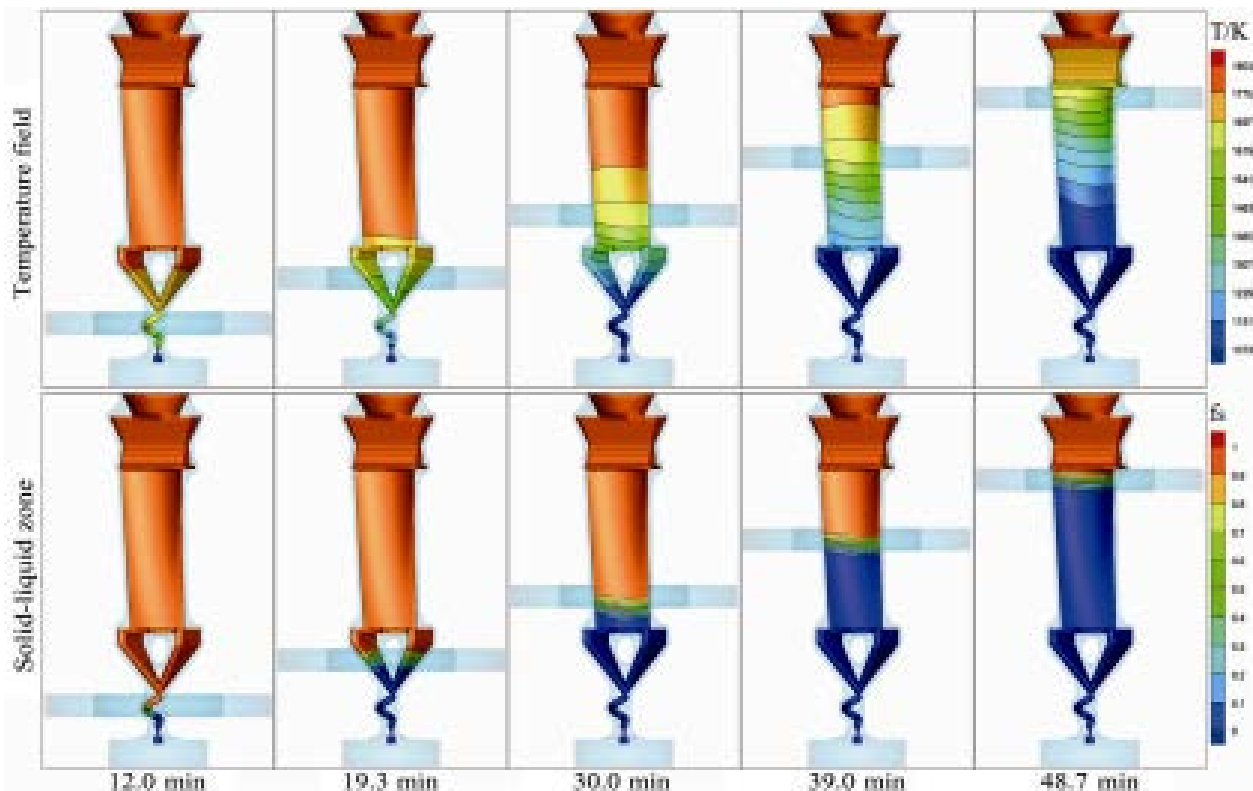

12.0 min   19.3 min   30.0 min   39.0 min   48.7 min

Fig. 12: Temperature and mushy zone fields of casting in scheme 1
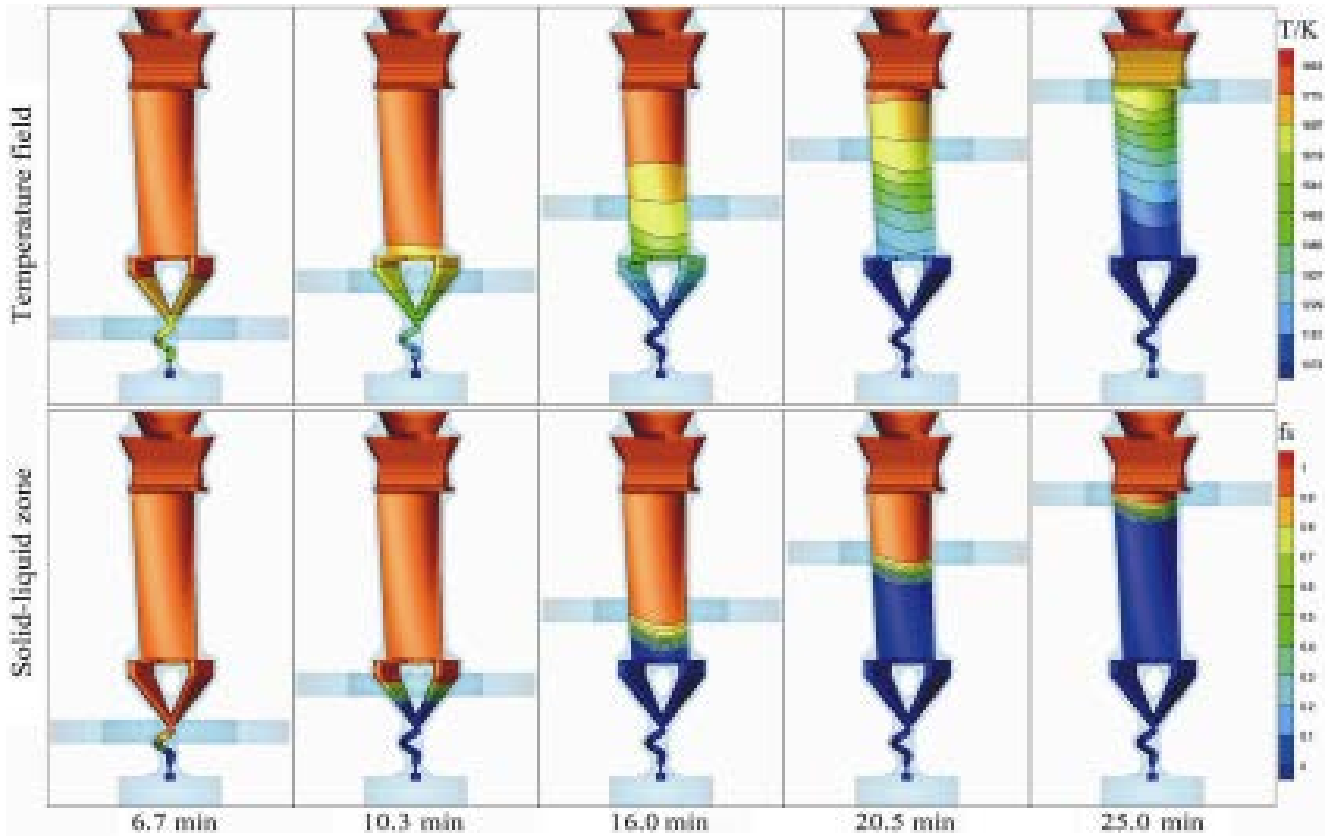
Fig. 13: Temperature and mushy zone fields of casting in scheme 2

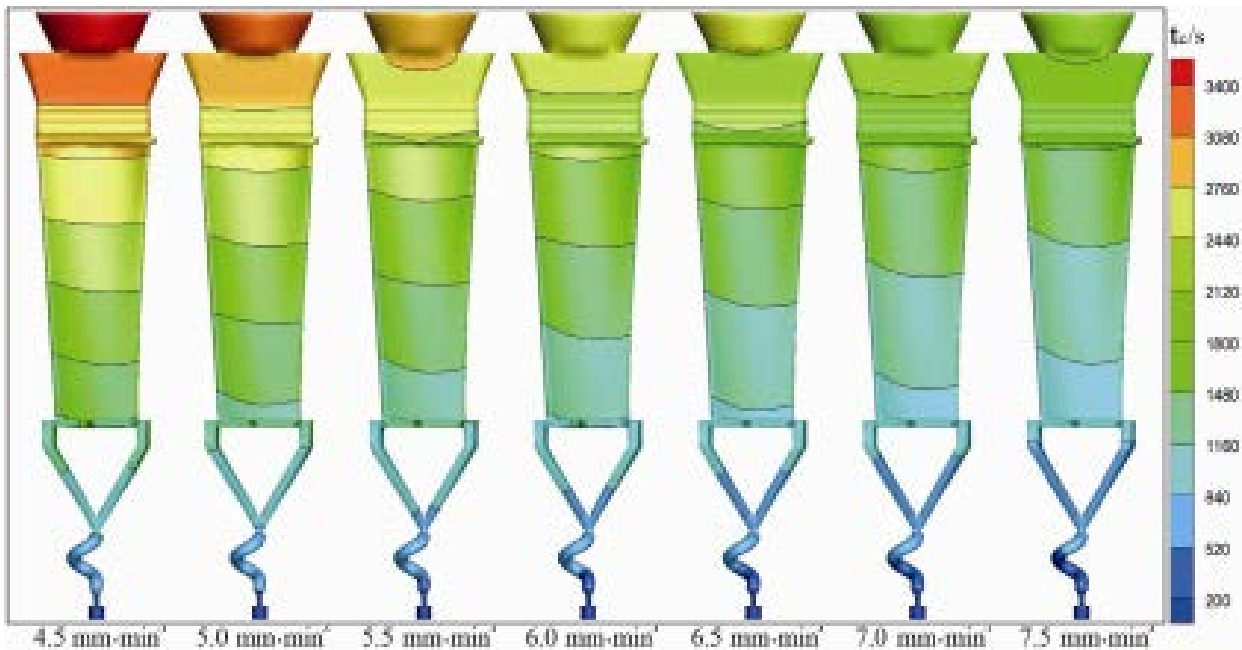**Fig. 14: Distributions of t_c under different withdrawing rates**

values appeared on the around of 6.0 mm·min⁻¹. Radiation heat transfer rate was slow under a low withdrawing rate, so the solidifying front was above the radiation baffle, which made a small temperature difference near the solidifying front. With the increase in withdrawing rate, the solidifying front was near the radiation baffle, so a large temperature difference could be generated nearby the solidifying front. However, when the withdrawing rate increased too much, the temperature difference became smaller as the solidifying front was under the radiation baffle.
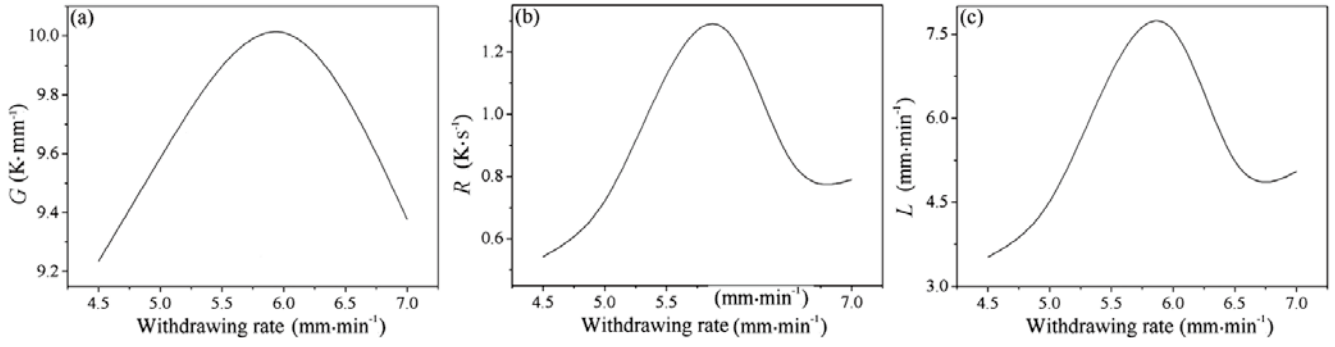
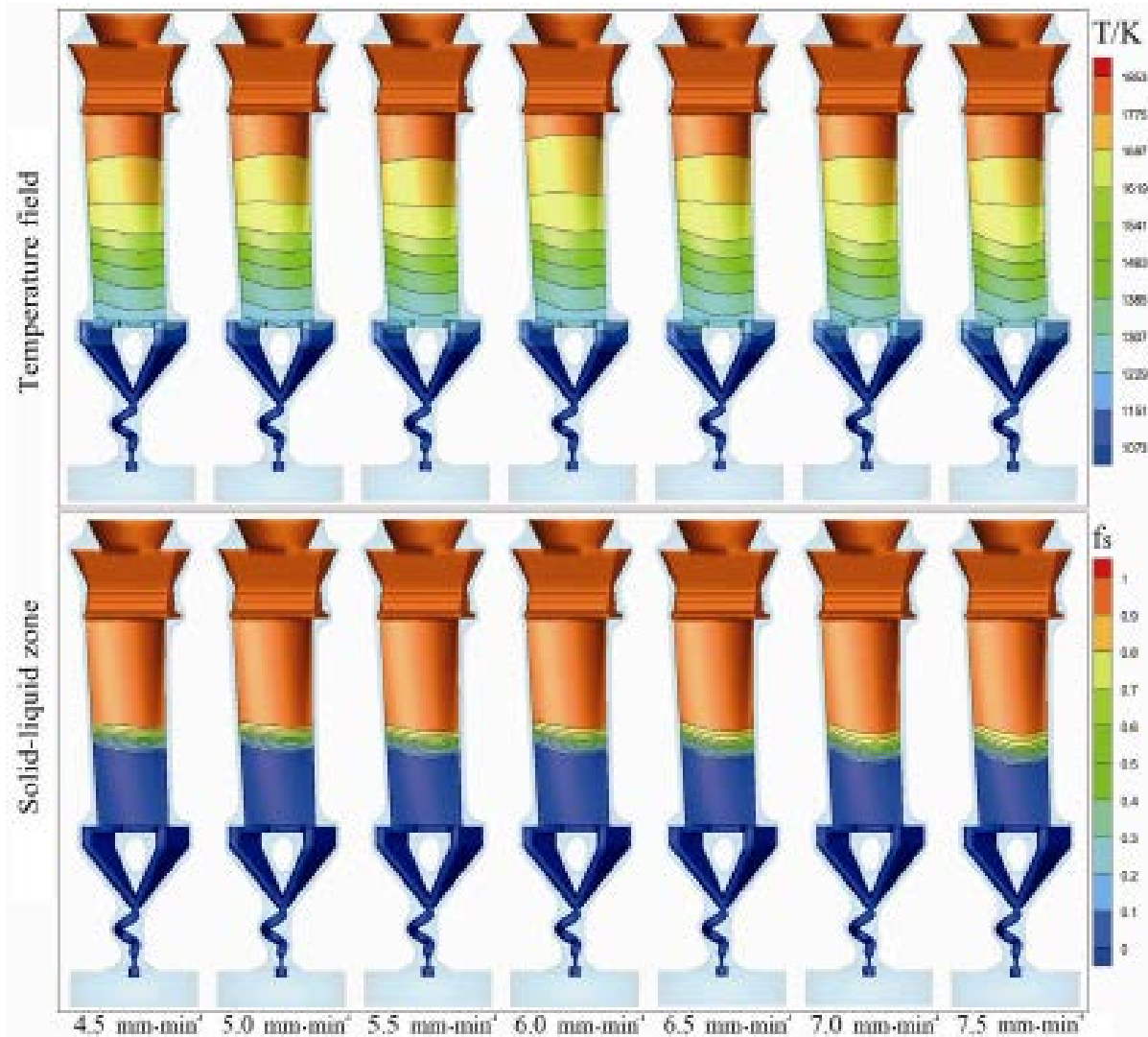Fig. 15: Comparisons of *G, R* and *L* under different withdrawing rates

Fig. 16: Temperature and mushy zone fields of casting in seven schemes when mushy zone reached the middle of blade

The situation when the mushy zone reached the middle of blade is supposed to reflect best the influence of withdrawing rate on deflected grain, and Figure 16 shows the temperature and mushy zone fields of casting in seven schemes under the situation. The solidifying front presents a concave distribution which is liable to cause deflected grain when the withdrawing rate exceeds 5.0 mm•min^{-1}.

Finally, based on the above analyses, 5.0 mm•min^{-1} is the most suitable withdrawing rate for the purpose of reducing the possibility of deflected grain, obtaining larger values of *G, R* and *L*, as well as improving the production efficiency possibly.

3 Conclusion

In this study, a radiation heat transfer model based on FEM was developed to calculate the radiation heat transfer in DS process, meanwhile, key technologies such as distinguishing boundaries automatically, local matrix and lumped heat capacity matrix, are also examined. On the basis of the model, more accurate shell boundary and calculation of radiation heat transfer can be achieved. The solidification processes of a superalloy turbine blade in HRS process with different withdrawing rates were computed, discovering that the solidifying front presented concave distribution which is liable to cause deflected grain with the increase in withdrawing rate. 5.0 mm·min^{-1} was determined to be the most suitable withdrawing rate, by comparing the situations when the mushy zone reached the middle of blade.

References

[1] Versnyder F I, Shank M E. The development of columnar grain and single crystal high temperature materials through directional solidification. Materials Science and Engineering, 1970, 6(4): 213–247.

[2] VerSnyder F L, Barlow R B, Sink L W, et al. Directional solidification in the precision casting of gas-turbine parts. Mod Cast, 1967, 52(6): 68–75.

[3] Fu H, Geng X. High rate directional solidification and its application in single crystal superalloys. Science and Technology of Advanced Materials, 2001, 2(1): 197–204.

[4] Zhou Y. Formation of stray grains during directional solidification of a nickel-based superalloy. Scripta Materialia, 2011, 65(4): 281–284.

[5] Zhou J X. Current status and development trend of casting numerical simulation technology. Foundry, 2013, 61(10): 1105–1115. (In Chinese)

[6] Hao L P, Tian W X, Zheng H L, et al. Progress in numerical simulation of directional solidification. Foundry, 2007, 56(7): 704–707. (In Chinese)

[7] Lu Y Z, Xi H J, Shen J, et al. Experimental and simulation study of directional solidification process for industrial gas turbine blades prepared by liquid metal cooling. Acta Metallurgica Sinica, 2015, 51(5): 603–611.

[8] Li Z, Zhang Y, Hu Z, et al. Numerical investigation of the effect of a crucible cover on crystal growth in the industrial directional solidification process for silicon ingots. Journal of Crystal Growth, 2014, 401: 291–295.

[9] Yu J, Xu Q Y, Li J R, et al. Numerical simulation of directional solidification process of multiple turbine blades of Ni-based superalloy. Acta Metallurgica Sinica, 2007, 43(10): 1113–1120.

[10] Yu J, Xu Q, Cui K, et al. Numerical simulation of solidification process on single crystal Ni-based superalloy investment castings. Journal of Materials Science & Technology, 2007, 23(1): 47–54.

[11] Schneider M C, Gu J P, Beckermann C, et al. Modeling of micro- and macrosegregation and freckle formation in single-crystal nickel-base superalloy directional solidification. Metallurgical and Materials Transactions A, 1997, 28(7): 1517–1531.

[12] Boettinger W J, Warren J A. Simulation of the cell to plane front transition during directional solidification at high velocity. Journal of crystal growth, 1999, 200(3): 583–591.

[13] Guo J, Li X, Su Y, et al. Phase-field simulation of structure evolution at high growth velocities during directional solidification of Ti55Al45 alloy. Intermetallics, 2005, 13(3): 275–279.

[14] Reinhart G, Gandin C A, Mangelinck-Noël N, et al. Influence of natural convection during upward directional solidification: A comparison between in situ X-ray radiography and direct simulation of the grain structure. Acta Materialia, 2013, 61(13): 4765–4777.

[15] Mitchell R A and Griffiths F D. The finite difference method in partial differential equations, 1st ed., Hoboken: John Wiley & Sons, 1980: 45–53.

[16] Dhatt G, Lefrançois E and Touzot G. Finite Element Method, 1st ed., Hoboken: John Wiley & Sons, 2012: 58–62.

[17] Hong Y W, Sun C B, Kang J W, et al. Numerical simulation of thermal stress during directional solidification of simple hollow turbine blades. Foundry, 2011, 60(8): 759–764. (In Chinese)

[18] Xue M, Cao L M, Liu S Z, et al. Simulation of temperature fields on ceramic core and ceramic shell during directional solidification process. Foundry, 2007, 56(3): 287–289. (In Chinese)

[19] Cui K, Xu Q Y, Yu J, et al. Radiative heat transfer calculation for superalloy turbine blade in directional solidification process. Acta Metallurgica Sinica, 2007, 43(5): 465–471.

[20] Pan D, Xu Q Y, Liu B C, et al. Modelling on directional solidification of superalloy blades with furnace wall temperature evolution. Acta Metallurgica Sinica, 2010, 46(3): 294–303.

[21] Erickson J S, Owczarski W A, Curran P M. Advances in fabricating aerospace structures process speeds up directional solidification. Metal Progress, 1971, 99(3):58–60.

[22] Higginbotham G J S. From research to cost-effective directional solidification and single-crystal production–an integrated approach. Materials Science and Technology, 1986, 2(5): 442–460.

[23] Chen T. Numerical Simulation of Casting Thermal stress based on finite element method and intelligent techniques. Ph.D. Thesis. Wuhan: Huazhong University of Science and Technology, 2013: 55–79.

[24] Qi L H, Jian L I U, Guan J T, et al. Damage prediction for magnesium matrix composites formed by liquid-solid extrusion process based on finite element simulation. Transactions of Nonferrous Metals Society of China, 2010, 20(9): 1737–1742.

[25] Cao L, Liao D M, Cao N M, et al. Temperature-Field Simulation Software Self-Development of Investment Casting Based on Finite Element Method. Foundry, 2014, 63(12). 1235–1240. (In Chinese)

[26] Wang C X. Finite Element Method, 1st ed., Beijing: Tsinghua University Press, 2003: 447–454.

[27] Inoue T, Funatani K, Totten G. Progress modeling for heat treatment: Current status and future development. Journal of Shanghai Jiaotong University, 2000, 5(1): 14–25.